Editors' Suggestion

Magnetic proximity effect in magnetic-insulator/heavy-metal heterostructures across the compensation temperature

Jackson J. Bauer,[1] Patrick Quarterman,[2] Alexander J. Grutter,[2] Bharat Khurana,[1] Subhajit Kundu,[3] K. Andre Mkhoyan,[3] Julie A. Borchers,[2] and Caroline A. Ross[1,*]

[1]*Department of Materials Science and Engineering, Massachusetts Institute of Technology, 77 Massachusetts Avenue, Cambridge, Massachusetts 02139, USA*

[2]*NIST Center for Neutron Research, National Institute of Standards and Technology, 100 Bureau Drive, Gaithersburg, Maryland 20899, USA*

[3]*Department of Chemical Engineering and Materials Science, University of Minnesota – Twin Cities, 421 Washington Avenue SE, Minneapolis, Minnesota 55455, USA*

(Received 1 June 2021; revised 7 August 2021; accepted 12 August 2021; published 1 September 2021)

The magnetic proximity effect in Pt and W thin films grown on $Dy_3Fe_5O_{12}$ (DyIG) is examined at temperatures above and below the magnetic compensation temperature of the ferrimagnetic insulator. Polarized neutron reflectometry indicates that the proximity effect is positive in Pt/DyIG both above and below the compensation temperature, and x-ray magnetic circular dichroism shows a weak positive W magnetization below compensation in W/DyIG. This demonstrates a qualitative difference compared to heavy metal/ferrimagnetic rare earth–transition metal alloys, where the proximity-induced magnetism of the heavy metal changes sign at the compensation temperature. Reflectometry, structural, and spin transport measurements show that depositing the heavy metal film on the ferrimagnetic insulator *in situ* without breaking vacuum avoids the formation of a low density interfacial layer between the Pt and DyIG.

DOI: 10.1103/PhysRevB.104.094403

I. INTRODUCTION

The magnetic proximity effect (MPE) occurs in heterostructures comprised of nonmagnetic heavy metals (HMs) and magnetic materials. A thin interfacial region in the nonmagnetic metal acquires an induced moment via exchange with the magnetic layer. Proximity effects have been studied in several nonmagnetic metals which are close to the Stoner criterion, including Pt [1–3], Pd [4,5], Ir [6], and W [6–8], coupled to a variety of magnetic materials including transition metals (Fe [4,9], Co [2,10,11], Ni [1,9]), chalcogenides [12,13], ferrimagnetic rare earth–transition metal alloys [14], and ferrimagnetic-insulator spinels [15,16] and garnets [3,7,17–23].

HM/magnetic heterostructures, particularly those including Pt, are of current technological interest. The spin current resulting from a charge current in the HM can be injected into the magnetic layer leading to current-induced switching [24,25], skyrmion generation and manipulation [26], and fast domain wall motion [27], and spin current injected from a magnetic layer into the HM can be detected by the inverse spin Hall effect. Magnetism induced in the HM via the MPE contributes to the magnetoresistance of the HM and couples to the magnetic moment of the ferromagnet, making MPE an important factor determining the behavior of HM/magnetic heterostructures, especially at low temperatures where MPE is stronger. In HM/magnetic metal heterostructures the MPE has been attributed to the magnetic polarization of the mobile conduction electrons. Studies of HM/rare earth–transition metal alloys have suggested that the MPE may be related to a Ruderman-Kittel-Kasuya-Yosida (RKKY) type interaction between the *d* electrons of the transition metal and the heavy metal, with the rare earth having little influence on the MPE [14,28]. However, in HM/magnetic-insulator bilayers, the lack of mobile electrons in the magnetic layer requires that the MPE have a different origin, likely related to a superexchangelike interaction with magnetic cations near the surface. First principles calculations in graphene/$Y_3Fe_5O_{12}$ [29] and Pt/$CoFe_2O_4$ [30] have shown that a magnetic insulator modifies the band structure of graphene or Pt to induce proximity effects via interactions with the Fe ions nearest the interface.

There have been several studies of MPE in heavy metals grown on the prototypical magnetic garnet, yttrium iron garnet (YIG), but disagreement exists about the strength of the MPE. For example Geprägs *et al.* did not observe any induced moment in Pt/YIG at 300 K whereas Lu *et al.* report a measurable MPE in Pt/YIG at 300 and 80 K [18,19,31]. Differences in MPE originate from the interface quality and growth method [31,32]. First principles calculations have shown that surface termination, vacancies, and crystallographic orientation in YIG can affect the strength of the MPE [33], and Jungfleisch *et al.* have shown surface cleanliness prior to Pt deposition can affect the spin mixing conductance by more than two orders of magnitude [34]. Intermixing between the magnetic layer and the HM can also lead to the formation of an interfacial magnetic alloy such as Fe_xPt_{1-x} [31]. In such alloys the HM moment originates from the polarization of HM atoms by magnetic species within the structure, as opposed to the case of MPE where polarization originates from an adjacent

*caross@mit.edu

magnetic layer, and the alloys are characterized by high Curie temperatures and a monotonic increase in magnetization with decreasing temperature [35,36].

Studying the MPE in heavy metals adjacent to multisublattice ferrimagnetic materials [37] near the magnetic compensation temperature (T_M) [38] provides insight into the origin of MPE. Changes in the sign and magnitude of the MPE through the compensation temperature have been examined in Pt/rare earth-transition metal alloy/Pt trilayers, where the induced Pt moment was found to couple parallel to the transition metal sublattice at all temperatures [14]. In rare earth–transition metal alloys, the transition metal dominates the electronic and magnetotransport properties. The rare earth $4f$ orbitals are highly localized and located well below the Fermi level, while the transition metal $3d$ conduction electrons more easily hybridize with the heavy metal [14,39,40]. This explains why the transition metal dominates the MPE, which changes sign at T_M.

Analogous experiments on MPE of HM/magnetic-insulator heterostructures are rare because the commonly studied ferrimagnetic oxides (YIG and $CoFe_2O_4$) do not exhibit compensation temperatures. Shao *et al.* [7]. examined MPE in W/TmIG (thulium iron garnet) bilayers, showing a negative MPE, i.e., antiparallel coupling of the W moment to the net TmIG moment above the compensation of $T_M = 75$ K, a temperature range where the magnetic moment of the garnet is dominated by the tetrahedral Fe^{3+} sublattice [7]. The MPE was not directly characterized below T_M, although Hall measurements suggested MPE changed sign below T_M. The existence of a T_M may indicate nonideal stoichiometry [41], since bulk TmIG does not show a compensation temperature. In contrast, Pt/YIG exhibits a positive MPE [42], suggesting that W and Pt exhibit opposite signs of MPE when coupled to magnetic insulators, the same trend seen in W and Pt coupled to magnetic metals [6].

These results motivate an examination of MPE in a HM/magnetic insulator both above and below T_M to better understand how the proximity magnetism of the HM couples to the ferrimagnet sublattices. Comparisons may be made with other interfacial magnetic phenomena such as spin transport at HM/magnetic-insulator interfaces. A sign change has been observed in the anomalous Hall effect–like (AHE) spin Hall magnetoresistance (SMR) in Pt/TbIG(terbium iron garnet)/gadolinium gallium garnet(GGG) films at T_M, and the spin mixing conductance has little dependence on the rare earth ion for several Pt/rare earth garnets [43–45], suggesting that spin transport across the HM/magnetic-insulator interface is dominated by the Fe sublattices.

MPE has been characterized by x-ray magnetic circular dichroism (XMCD [1,3,11]) and polarized neutron reflectometry (PNR [7,9]) to measure the magnetic moment of the HM, and by indirect measurements based on magnetoresistance (MR [17,46]). In particular, PNR allows for extraction of depth dependent composition and the in-plane component of the magnetization through specular reflection of spin-polarized neutrons. This allows for simultaneous, quantitative determination of the physical, interfacial, and magnetic structure [47,48]. XMCD complements PNR by providing elemental specificity due to the tunable energy of synchrotron radiation.

In this paper we report the MPE of Pt/dysprosium iron garnet (DyIG) heterostructures measured using PNR both above and below the compensation temperature. DyIG was selected due to its easily accessible compensation temperature of ∼220 K in bulk, and because it exhibits an in-plane magnetic easy axis when grown epitaxially on gadolinium gallium garnet (GGG) substrates [38,44] which is convenient for PNR characterization. We compare these results with XMCD measurements of MPE in W/DyIG heterostructures. Further, we characterize the effect of *ex situ* vs *in situ* deposition of the HM by comparing MPE in Pt/DyIG in which the Pt was deposited with or without breaking vacuum after growth of the DyIG.

II. METHODS

DyIG (111) films were grown on a GGG substrate by pulsed laser deposition (PLD) from a bulk DyIG target made by solid oxide sintering methods [49]. A 248-nm KrF excimer laser with a fluence of $2.0\,J/cm^2$ and repetition rate of 10 Hz was used to ablate the target. The DyIG film was grown in 150-mTorr (20 Pa) O_2 at 650 °C and cooled in 150 mTorr O_2 at a rate of 10 °C/min. After cooling the DyIG to room temperature, Pt was deposited *in situ* by DC magnetron sputtering in the same chamber with an argon pressure of 5 mTorr (0.7 Pa) and 30 W power, at a base pressure of 1×10^{-6} Torr (1×10^{-4} Pa). W (β phase) was sputtered *in situ* at 5 mTorr (0.7 Pa) and 100 W power at room temperature. For comparison, another sample of DyIG/GGG underwent structural and magnetic characterization before it was cleaned via sonication in acetone and isopropyl alcohol immediately prior to *ex situ* Pt deposition in a separate sputter chamber (5×10^{-6} Pa base pressure, 0.7-Pa Ar pressure, 50 W power). High resolution x-ray diffraction (HRXRD) and x-ray reflectivity (XRR) were collected with a Bruker D8 Discover diffractometer with a Cu $K\alpha$ source. Magnetic hysteresis loops were measured with a Digital Measurement Systems Vibrating Sample Magnetometer (VSM) Model 1660. Anomalous Hall effect-like (AHE) spin Hall magnetoresistance (SMR) was measured with a standard lock-in technique [50] after patterning the Pt/garnet bilayer into Hall crosses (200 μm × 20 μm) using optical lithography and ion beam etching.

PNR measurements were performed at the NIST Center for Neutron Research using the Polarized Beam Reflectometer. Incident neutrons were polarized parallel or antiparallel to the 200-mT applied in-plane magnetic field, and the non-spin-flip reflectivity cross sections (R^{++} and R^{--}) were collected. Reflectivity data were collected at 10, 200, 240, and 300 K. A model consisting of the structure GGG/DyIG/Pt/Pt2(/surface adsorbate) was developed, and the data were fit simultaneously so that the thickness and interface roughness of the layers were consistent across the temperature range, allowing only the magnetic components to vary. A thin, low scattering length density surface layer was included with the 10-K model fitting to account for gases that had condensed on the sample surface during cooling. The model subdivides the Pt into two layers (Pt and Pt2) which were allowed to have slightly different scattering length densities (SLDs) and interface widths at 10 K, which we attribute to the gases adsorbing in the less dense and more columnar upper Pt2 layer. The thicknesses, SLDs, and scattering length densities of the Pt and Pt2 layers

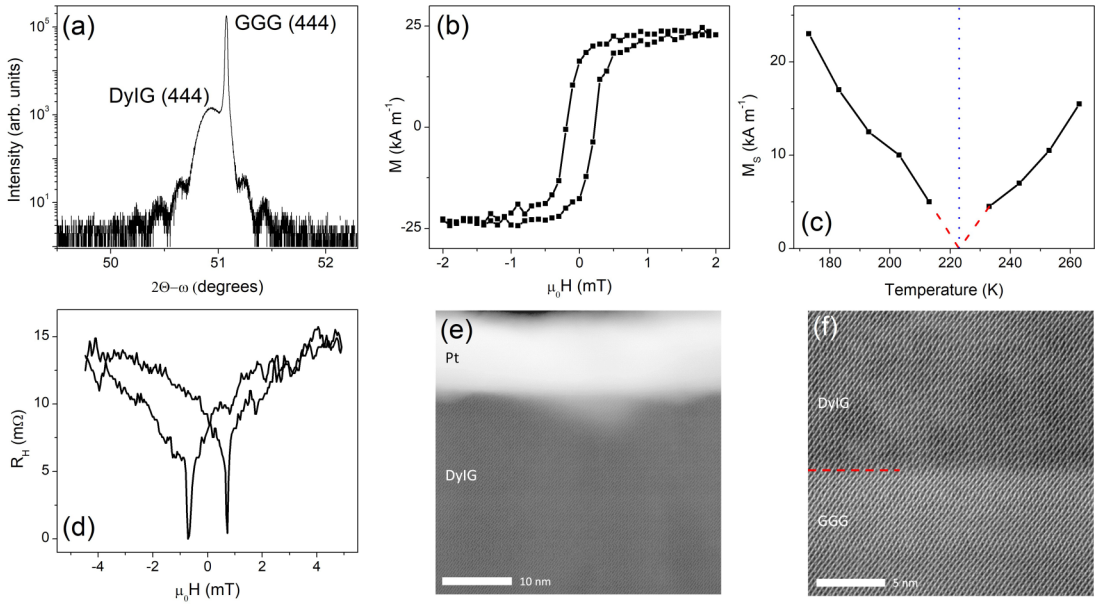

FIG. 1. (a)–(c) Characterization of the *in situ* grown Pt(9 nm)/DyIG(54 nm)/GGG sample. (a) High-resolution XRD of the DyIG/GGG (444) reflection. (b) In-plane room temperature VSM hysteresis loop. (c) Saturation magnetization vs temperature for DyIG/GGG; red dashed lines indicate extrapolation from experimental data. Blue vertical dashed line indicates the bulk value of T_M. (d) In-plane room temperature AHE-like SMR on the *in situ* grown W(5 nm)/DyIG(42 nm)/GGG sample. ADF-STEM images of the (e) Pt/DyIG and (f) DyIG/GGG interfaces of the *in situ* grown Pt(9 nm)/DyIG(54 nm)/GGG sample.

are fixed in the 200-, 240-, and 300-K models. Spin asymmetry was calculated as the normalized difference between the non-spin-flip polarization states $(R^{++} - R^{--})/(R^{++} + R^{--})$. The REDUCTUS and REFL1D software packages were used to reduce the raw data and fit the models, respectively [51,52].

XMCD measurements were done at the Advanced Photon Source at Argonne National Laboratory using the 4-ID-C beamline for the Fe $L_{2,3}$, Dy $M_{4,5}$, and O K edges, and the 4-ID-D beamline for the Pt L_2 and W L_3 edges. A ±0.5-T (Fe, Dy, O) or ±0.05-T (W, Pt) in-plane field was applied to saturate the samples. Total fluorescence yield (TFY) data were collected at all edges. XMCD measurements were performed by alternating both photon helicity and magnetic field direction so that the x-ray absorption spectra (XAS) was collected for all four configurations: $(+_{\text{Photon}}+_{\text{Field}})$, $(+_{\text{Photon}}-_{\text{Field}})$, $(-_{\text{Photon}}+_{\text{Field}})$, and $(-_{\text{Photon}}-_{\text{Field}})$. S/TEM sample preparation was done using a FEI Helios Nanolab G4 dual-beam FIB. The Pt/DyIG/GGG wafer was sputtered with a 40-nm layer of carbon to protect the top surface during FIB cross-section lamella cutting. S/TEM imaging and EDX mapping were performed using an aberration-corrected FEI Titan G2 60–300 STEM equipped with a Schottky extreme field emission gun, CEOS DCOR probe corrector, and a Gatan Enfinium ER spectrometer. STEM measurements were carried out at 200 kV accelerating voltage, 25.5 mrad probe convergence angle, and at 130 mm camera length.

III. RESULTS

A. Structural and magnetic characterization

High resolution x-ray diffraction around the DyIG (444) reflection of an *in situ* grown Pt(9 nm)/DyIG(54 nm)/GGG film is shown in Fig. 1(a), indicating high crystalline quality of the DyIG and a larger out of plane lattice parameter than that of the substrate. Reciprocal space maps (RSMs) of similar films, as well as TEM images, show a coherent interface between DyIG and GGG. The bulk lattice parameter of DyIG (1.2405 nm) exceeds that of GGG (1.2376 nm) and the film is under in-plane compressive strain [43,45]. Annular dark-field scanning transmission electron microscopy (ADF-STEM) images show a sharp interface transition between the DyIG and Pt layers [Fig. 1(e)], with a rougher top surface of the Pt. The *in situ*, low energy Pt deposition via sputtering results in little interdiffusion and disorder at the surface of the DyIG film, similar to other results in Pt/YIG and Pt/TmIG [53,54]. Previous TEM of Pt/garnet where the Pt has been deposited *ex situ* have shown a darker layer or voids indicating the presence of carbon-based contamination between the garnet and platinum, which limits the direct contact between the Pt and magnetic layer [55]. At the bottom interface, an epitaxial growth of the DyIG on GGG is evident, with no observable dislocations or defects [Fig. 1(f)].

The TEM and PNR both indicate the presence of a rough upper surface of the sputtered Pt layer, dubbed Pt2. The sputtering source is mounted at an angle of 45 ° to the substrate normal, resulting in a shadowing effect that leads to increased roughness compared to normal incidence deposition, even when the sample is rotated during growth. The roughness and waviness in the Pt layer seen in the TEM is larger than observed in the PNR and AFM, which we attribute to partial delamination occurring during the focused ion beam (FIB) milling used for sample preparation.

A typical room temperature VSM in-plane hysteresis loop in Fig. 1(b) indicates a saturation magnetization of 25 kA/m and coercivity of 0.3 mT. The in-plane easy axis is a result of both the shape anisotropy and the magnetoelastic anisotropy

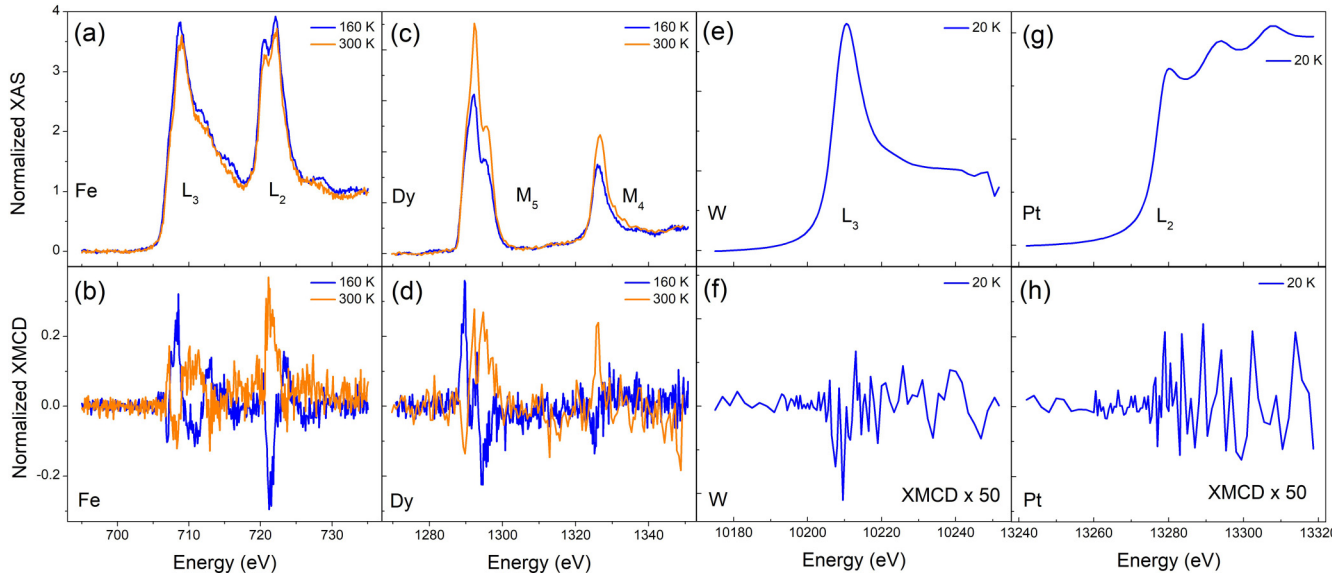

FIG. 2. XAS and XMCD for (a), (b) Fe $L_{2,3}$, (c), (d) Dy $M_{4,5}$, (e), (f) W L_3, (g), (h) Pt L_2 edges. Panels (a)–(f) were collected on the *in situ* grown Pt/DyIG/GGG sample and (g) and (h) on the *in situ* W/DyIG/GGG sample.

[44]. The magnetostriction coefficient λ_{111} is negative and favors in-plane magnetization when the film is in compression in plane. The compensation temperature of the Pt/DyIG/GGG bilayer was 220 K [Fig. 1(c)], in agreement with the value for bulk DyIG. This differs from the T_M of 190 K measured for DyIG/GGG in our recent work [44] which was likely lower due to a processing-dependent change in Dy:Fe ratio [43,56].

The anomalous Hall effect-like (AHE) spin Hall magnetoresistance (SMR) was measured in plane on an *in situ* grown W(5 nm)/DyIG(42 nm)/GGG Hall cross. The two minima in Fig. 1(d) correspond to the coercivity in the patterned film as the magnetization reverses in plane. The coercivity in both VSM hysteresis loops and SMR is low, $\mu_0 H_c = 0.3$ and 0.8 mT respectively, indicating few pinning sites impeding domain wall motion. The SMR data illustrates spin transport at the interface of *in situ* W/DyIG which is relevant for device applications of garnet/heavy metal heterostructures.

B. X-ray magnetic circular dichroism

X-ray magnetic circular dichroism enables the magnetic characterization of garnets and heterostructures with both elemental and site specificity, making it possible to compare the orientation of the magnetic moment of the Pt to that of the octahedral and tetrahedral Fe and the rare earth sublattices. First, dichroism was measured at the Fe $L_{2,3}$ and Dy $M_{4,5}$ edges above and below T_M for a Pt(9 nm)/DyIG(54 nm)/GGG sample deposited simultaneously with the sample used for the PNR measurements. The pre-edge region of the x-ray absorption spectra [XAS, Figs. 2(a), 2(c), 2(e), and 2(g)] was set to zero and the post-edge region of the data was scaled to 1. The XMCD was scaled by the same factor as the XAS. The signs of the Fe [Fig. 2(b)] and Dy [Fig. 2(d)] XMCD reverse from 160 to 300 K, as the DyIG passes through its compensation temperature. The Dy plus octahedral Fe have the larger moment below T_M, while the tetrahedral Fe dominates above T_M. No XMCD is observed at the O *K* edge, as expected for the garnets (see the Supplemental Material [57]).

Measurements of the Pt L_2 edge XMCD [Fig. 2(h)] detected no dichroism above the noise floor across a temperature range 20–240 K. While detection of any Pt XMCD may have been inhibited by interference from the Ga $K\alpha$ peaks at the stronger Pt L_3 edge [58], it is more likely due to averaging over the entire 9-nm-thick Pt layer. The TFY data sample the entire 9-nm film to some degree, and the detected XMCD magnitude indicates the average moment per Pt. The lack of a clear dichroism signal likely indicates that any MPE must be confined to the first few nm near the interface. This constraint is considered in the PNR modeling.

XMCD was also probed from a W(5 nm)/DyIG(42 nm)/GGG heterostructure at the W L_3 edge. A weak dichroism [Fig. 2(f)] was detected at 20 K, but not at 200 K. This temperature dependence is attributed to the lower maximum temperature of the W MPE, which has been reported previously [7]. The integrated W XMCD is consistent with a positive MPE, while previous measurements of Co-W alloys found that the induced moment of the W is antiparallel to the Co moment [8]. A positive MPE in W/DyIG would contrast with the negative MPE observed in W/TmIG by Shao *et al.* at the W N_3 edge [7]. These divergent results may originate from differences in Fe site occupancy in the garnet films. The surface sensitive total electron yield XMCD measurements of Shao *et al.* at the Fe L_3 edge revealed a larger contribution from the tetrahedral Fe site relative to the octahedral Fe compared to previous work on TmIG films without a compensation temperature [45].

By comparing the amplitude of the normalized XMCD signal in Fig. 2(f) with that of literature values [8,18], an estimate of the W moment can be obtained. The signal obtained here is approximately three times lower than that of Figeuroa *et al.* [8], indicating a moment of at most 0.009 μ_B/W atom. Note that this value assumes a uniform magnetization distribution within the W, which is unlikely for an MPE. More likely, any

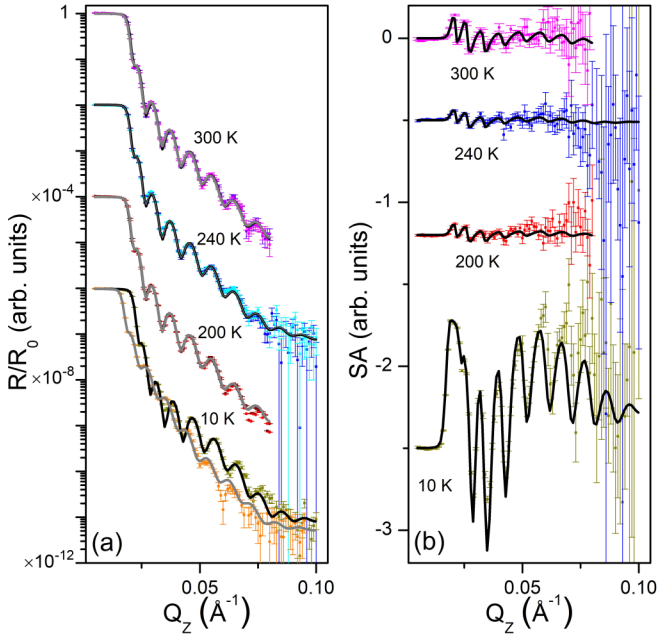

FIG. 3. (a) Fitted polarized neutron reflectometry curves and (b) spin asymmetry of *in situ* Pt(9 nm)/DyIG(54 nm)/GGG at 10, 200, 240, and 300 K. Vertically offset for clarity. Error bars are representative of 1σ.

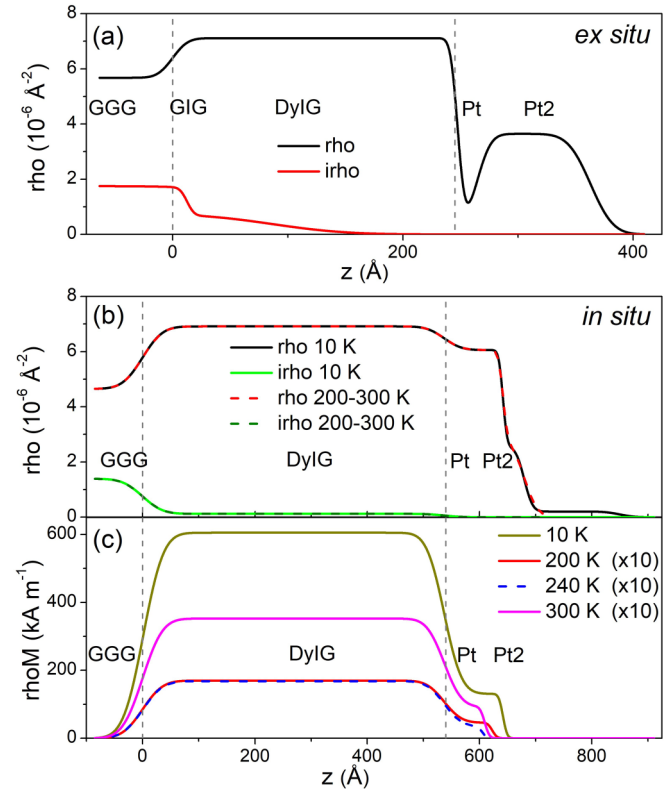

FIG. 4. Structural scattering length density profile of (a) *ex situ* and (b) *in situ* grown Pt(9 nm)/DyIG(54 nm)/GGG. rho and irho represent the real (density) and imaginary (absorption) components of the structural SLD. (c) Magnetic SLD of *in situ* sample, representing the magnetization.

net moment is concentrated near the interface, but a more accurate calibration would require a detailed depth profile. Using the published value of the paramagnetic susceptibility of W [59], the 0.05-T applied field results in a paramagnetic moment of $\sim 4 \times 10^{-7}\,\mu_B$/W atom across the temperature range of interest, i.e., paramagnetism cannot account for the measured W moment.

C. Polarized neutron reflectometry

Polarized neutron reflectometry is sensitive to the depth dependence of the composition, density, interface roughness, and in-plane component of the magnetization. PNR was collected on an *in situ* grown Pt/DyIG/GGG film at a low temperature where the MPE is expected to be the strongest (10 K), just below T_M (200 K), just above T_M (240 K), and at 300 K. Based on previous PNR studies of garnet thin films [44,60,61], a four-layer model was developed that incorporated an interdiffused region with the GGG substrate with an interface width of <5 nm, consistent with TEM. The reflectivity and fitted curves are shown in Fig. 3(a). The real and imaginary scattering length densities (SLDs) for GGG were fixed to the theoretical values calculated from bulk GGG properties. A satisfactory agreement is obtained across the data range, with $\chi^2 = 10.24$. The error bars become large at high Q_Z due to the signal approaching the background noise level. The spin asymmetry [Fig. 3(b)] highlights the magnetism in the system demonstrating that the model accounts well for both the structural and magnetic components.

The depth profiles (Fig. 4) for the real and imaginary components of the structural SLD (rho and irho, respectively, representing density and absorption) show constant values within the DyIG and Pt layers, close to the calculated bulk values. The difference in the nuclear SLD profiles for the Pt and Pt2 layers between 10 K and higher temperature is very small, and the surface layer is only necessary for fitting at 10 K to account for adsorbed gases. The irho profile shows neutron absorption is significant only in the GGG substrate, as expected for this heterostructure. Perhaps the most important feature is the smooth and narrow transition between the DyIG and Pt layers, indicating a clean interface with intimate contact between the magnetic insulator and heavy metal. The Pt2 layer proved to be necessary to account for the roughness of the top of the Pt. This rough, lower density Pt layer is corroborated by TEM.

A comparison is shown in Fig. 4 with a Pt/DyIG structure with the Pt deposited *ex situ* after the DyIG film was characterized [Fig. 4(a) and Supplemental Material Figs. S13 and S14 [57]]. There is a large decrease in the SLD at the surface of the DyIG indicating the presence of a low density region and implying less direct contact between the Pt and the garnet surface. The interfacial contamination also added a great deal of complexity to the fitting of the data to account for the sharp drop in SLD. Due to this, several degenerate solutions to the magnetic SLD were obtained which were not physically realistic. Previous studies have also observed a dip in the SLD between the garnet and Pt when the metal is deposited *ex situ*, due to the formation of a binary rare-earth oxide or carbon-based contamination [60,62]. Alternative PNR models of the *ex situ* deposited sample are presented in Supplemental

TABLE I. Table of χ^2 values, MPE magnitude, and MPE depth adjacent to the interface for the four models of the *in situ* Pt/DyIG/GGG film, listed in the order presented in the text. The magnetism for the exponential decay model follows an exponential profile, so the μ_B/Pt atom values are calculated as an average over the first nm from the interface.

Description of model	χ^2	Temperature (K)	μ_B/Pt atom (2σ)	MPE depth (nm) (2σ)
Constrained structural model [Figs. 3, 4(b) and 4(c)]	10.24	10	0.22 ± 0.01	9.6 ± 0.2
		200	0.007 ± 0.003	4.4 ± 2.0
		240	0.005 ± 0.004	1.8 ± 2.0
		300	0.014 ± 0.005	2.2 ± 2.0
MPE constrained to maximum depth of 3 nm (Figs. S5 and S6)	10.54	10	0.129 ± 0.034	2.8 ± 0.2
		200	0.037 ± 0.037	1.3 ± 1.2
		240	0.008 ± 0.042	1.4 ± 1.4
		300	0.030 ± 0.021	2.0 ± 1.1
MPE constrained to exactly 3 nm, structure relaxed (Figs. S7 and S8)	9.71	10	1.080 ± 0.024	3.0
		200	0.027 ± 0.007	3.0
		240	0.026 ± 0.008	3.0
		300	0.057 ± 0.009	3.0
Constrained structure, no MPE (Figs. S9 and S10)	13.30			
Exponential decay of MPE (Figs. S11 and S12)	10.20	10	0.939 ± 0.024	5.6 ± 0.1
		200	0.035 ± 0.009	0.2 ± 0.1
		240	0.038 ± 0.011	0.2 ± 0.1
		300	0.076 ± 0.015	0.5 ± 0.1

Material Figs. S15–S18 providing justification for the inclusion of the interdiffused GIG layer and the intermediary Pt layer. Table S1 of the Supplemental Material [57] shows that the model presented in Figs. 4(a), S13, and S14 that includes these features represents the best fit.

The magnetization profiles determined from PNR fitting are shown in Fig. 4(c). The magnetization in the DyIG layer shows negligible dead layers at the top and bottom surfaces, with saturation values that correspond well to magnetometry data at 200, 240, and 300 K, and to prior data at 10 K [38]. The model used for fitting the data allowed for the Pt layer to be magnetic, and to couple parallel or antiparallel to the DyIG magnetism, with independent values of magnetic moment at each temperature. A top magnetic dead layer in the Pt was also incorporated to account for the MPE existing only near the garnet interface. A paramagnetic contribution from the GGG substrate was also included, which varies as $1/T$.

Using this model, a positive MPE in Pt was detected at 10 and 300 K. The MPE at 10 K yields $0.22\,\mu_B/\text{Pt} \pm 0.01\,\mu_B/\text{Pt}$ atom (2σ), comparable to other reports of induced magnetism in Pt at low temperatures [1,63]. At 300 K the MPE strength is $0.014\,\mu_B/\text{Pt} \pm 0.005\,\mu_B/\text{Pt}$ atom (2σ). At 200 and 240 K, it is not possible to say there is a measurable MPE due to the low MPE strength and the overlap of the uncertainty with zero. However, the fit is inconsistent with a negative MPE at any of the four temperatures. The PNR was measured under a 200-mT in-plane field, which is not strong enough to affect the orientation of the Pt moment with respect to the DyIG moment (previous work on the MPE has been measured in fields $> 1\,\text{T}$) [6]. As the MPE is positive above and below compensation, we conclude that Pt/DyIG does not show a sign change in the Pt MPE, in contrast to the Pt MPE in Pt/rare earth transition metal bilayers [14].

The fitted magnetization profile at 10 K in Fig. 4(c) suggests that nearly all of the Pt is magnetic at low temperatures. This is not consistent with the known exponential decay of MPE away from the interface [58], nor with the XMCD measurements described above on an identical heterostructure which did not demonstrate any dichroism at 20 K, attributed to the large thickness of the Pt layer. To examine this further, the 10-K data were fit independently of the other temperatures, and the penetration depth of the MPE converged to ~3 nm into the Pt layer (Supplemental Material Figs. S3 and S4). Using this information, we restricted the depth of the MPE to a maximum of 3 nm and refit the data at all temperatures, which resulted in a slightly worse agreement with to the reflectometry data (Supplemental Material Figs. S5 and S6). To improve the structural fit, a third model was generated that allowed the DyIG/GGG and Pt/Pt2 interface widths to vary at 10 K and fixed the depth of the MPE at 3 nm. The justification for this is to account for a misalignment at high Q_Z at low temperature and to improve the value of χ^2 obtained (Supplemental Material Figs. S7 and S8). The χ^2 values, MPE values, and MPE depths from each model are shown in Table I.

When comparing alternative models, the two key results that the MPE is positive at 10 and 300 K and that the model does not indicate a negative MPE at any of the measured temperatures are robust. The models used in this study are more sensitive to the total Pt moment in the system than to the distribution of the moment in the Pt layer. This is particularly evident at 10 K, where restricting the MPE to a depth of 3 nm increases the Pt moment to an unphysically large value ($1.08\,\mu_B/\text{Pt atom}$). The true distribution of the Pt moment is most likely a middle ground between these two models, decaying exponentially away from the interface.

The true distribution of the Pt moment most likely decays with distance from the interface. To explore this, an additional model was created in which there is an interfacial Pt layer that has a magnetization falling off exponentially from the DyIG interface. We find that the resulting fits (Supplemental Material Fig. S11) are nearly identical to those shown in Fig. 3 both in χ^2 and quality of fit by eye. The magnetic scattering length density profiles for the slab [Fig. 4(c)] vs exponential decay (Supplemental Material Fig. S12) also converge

to strikingly similar models, which suggests we are unable to distinctly select one model over the given Q range and data uncertainties, and the two fits cannot be meaningfully distinguished.

Finally, a model without an MPE in the Pt layer was also considered (Supplemental Material Figs. S9 and S10). This results in a higher value of χ^2 and a lower quality fit to the reflectometry data. While the effect of the proximity magnetism on the model is strongest at 10 K, it is also necessary at 300 K to obtain the best fit to the data. At 200 and 240 K we cannot exclude the possibility of an MPE, but detection is below the sensitivity of our model.

IV. DISCUSSION

PNR measurements on Pt/DyIG above and below the compensation temperature demonstrate that the MPE is positive, and does not change sign across T_M. At 200 and 240 K, any MPE was at or below the detection limit, but the model is not consistent with a negative MPE. These results suggest that the MPE scales with the total magnetization of the DyIG, and the MPE is lower at 200 and 240 K than at 300 K because the magnetization of the DyIG is small near T_M. A threshold garnet magnetization may be required to observe an MPE in Pt/garnet, similar to reports on Pt/transition metal bilayers [64].

XMCD measurements on W/DyIG suggest that the MPE is also positive below T_M. MPE was not detectable at higher temperatures near T_M, consistent with the lower temperature onset of MPE in W compared to Pt.

The result for Pt/DyIG that MPE is positive above and below T_M is in contrast to HM/rare-earth transition metal alloys, where the MPE tracks the moment of the transition metal. This suggests a different mechanism exists for the MPE in HM/magnetic insulators compared to HM/ferromagnetic metals. The cations at the surface of the magnetic insulator interact via a superexchangelike mechanism with the heavy metal, as there are no conduction electrons in the insulator to mediate RKKY-like exchange coupling. The exact surface termination of the DyIG film is unknown, but closely spaced planes in the garnet lattice parallel to (111) contain octahedral sites or tetrahedral plus dodecahedral sites, and (111) facets with even a small roughness will exhibit all three sites at the surface. Interaction between the Pt and all three sublattices in the garnet could make the MPE sensitive to the net moment of the garnet instead of the moment of an individual sublattice. As a result the MPE does not change sign across the compensation temperature, but has a lower magnitude near the compensation temperature than it does at room temperature.

At low temperatures, the rare-earth iron garnets exhibit magnetic ordering different from a collinear state, such as canting of the rare-earth ion moments [65,66] or a double-umbrella structure [67]. Canting has also been observed close to the magnetic compensation temperature [65,68]. However, the modest canting angles (15 ° according to Lahoubi *et al.* [66]) and the large magnetic moment of the Dy^{3+} support the proposed exchange interaction with the Pt.

The PNR and XMCD data do not distinguish whether the magnetism in the HM arises from MPE originating from the garnet layer, or from alloying of magnetic species into the HM to form an interfacial layer of Fe_xPt_{1-x} or Fe_xW_{1-x}, for example. However, based on the nonmonotonic change in the magnitude of the magnetism in the Pt layer, a MPE from the garnet layer is the more likely origin, since the magnetic moment of Fe_xPt_{1-x} increases monotonically with decreasing temperature. The measured MPE is smallest at the intermediate temperatures of 200 and 240 K, consistent with the conclusion that the MPE scales with the net magnetization of the DyIG.

PNR and TEM clearly indicate that *in situ* deposited heavy metal layers are critical for obtaining high quality interfaces. The precipitous drop in scattering length density between the Pt and DyIG layers is eliminated by *in situ* deposition, resulting in a sharper interface. The difference in interface quality is a possible explanation for the conflicting reports on the existence of the MPE in Pt/YIG and $Pt/CoFe_2O_4$ heterostructures. This is reflected in the greatly simplified PNR model of the *in situ* heterostructure. More broadly, differences in the stoichiometry, site occupancy, and surface chemistry in garnet films have a large impact of the film properties. For instance, in both TbIG and TmIG films T_M values far from the bulk value have been reported, which in the case of TbIG has been attributed to a deviation from the ideal Tb:Fe = 3:5 ratio composition [7,43]. A difference in relative site occupancy of the cations may also have an impact on the strength or even the relative orientation of the MPE in Pt/iron garnets.

V. CONCLUSIONS

In summary, PNR measurements have conclusively demonstrated that the magnetic proximity effect in Pt/DyIG is positive and does not change sign across the compensation temperature. XMCD measurements place limits on the depth of the MPE in Pt/DyIG and is consistent with a weak, positive MPE in W/DyIG at 20 K. The result that the MPE tracks the net moment of the system suggests a different origin for MPE in HM/magnetic insulators compared to the RKKY interaction reported to cause MPE in HM/ferrimagnetic metals. For *in situ* deposited Pt/DyIG, the magnetic and structural SLD profiles derived from PNR match well to magnetometry and film thickness measurements. However, *ex situ* deposited Pt/DyIG shows a more complex layer structure with a low density interfacial layer between the Pt and DyIG evident in PNR and TEM. This provides strong evidence that *in situ* deposition is critical for fabricating high performance spintronic heterostructures. The same sign of the proximity effect above and below the compensation temperature also has implications for further fundamental and technological work on the relationship between magnetism in ferro/ferrimagnets and heavy metals.

ACKNOWLEDGMENTS

The authors thank Prof. R. Kawakami for helpful discussions. We gratefully acknowledge partial support from NSF Grant No. DMR-1808190, DARPA TEE Program, and SMART, an nCORE Center of the Semiconductor Research Corporation. This work made use of the Shared Experimental Facilities supported in part by the MRSEC Program of the National Science Foundation under Award

No. DMR-1419807. This research used resources of the Advanced Photon Source, a U.S. Department of Energy (DOE) Office of Science User Facility operated for the DOE Office of Science by Argonne National Laboratory under Contract No. DE-AC02-06CH11357. Certain commercial equipment and instruments are identified in this paper to foster understanding. Such identification does not imply recommendation or endorsement by the National Institute of Standards and Technology, nor does it imply that the equipment identified is necessarily the best available for the purpose.

[1] F. Wilhelm, P. Poulopoulos, G. Ceballos, H. Wende, K. Baberschke, P. Srivastava, D. Benea, H. Ebert, M. Angelakeris, N. K. Flevaris, D. Niarchos, A. Rogalev, and N. B. Brookes, Phys. Rev. Lett. **85**, 413 (2000).

[2] S. Ferrer, J. Alvarez, E. Lundgren, X. Torrelles, P. Fajardo, and F. Boscherini, Phys. Rev. B **56**, 9848 (1997).

[3] B. F. Miao, S. Y. Huang, D. Qu, and C. L. Chien, Phys. Rev. Lett. **112**, 236601 (2014).

[4] J. J. Hauser, Phys. Rev. **187**, 580 (1969).

[5] J. Vogel, A. Fontaine, V. Cros, F. Petroff, J.-P. Kappler, G. Krill, A. Rogalev, and J. Goulon, Phys. Rev. B **55**, 3663 (1997).

[6] F. Wilhelm, P. Poulopoulos, A. Scherz, H. Wende, K. Baberschke, M. Angelakeris, N. K. Flevaris, J. Goulon, and A. Rogalev, Phys. Status Solidi Appl. Res. **196**, 33 (2003).

[7] Q. Shao, A. Grutter, Y. Liu, G. Yu, C. Y. Yang, D. A. Gilbert, E. Arenholz, P. Shafer, X. Che, C. Tang, M. Aldosary, A. Navabi, Q. L. He, B. J. Kirby, J. Shi, and K. L. Wang, Phys. Rev. B **99**, 104401 (2019).

[8] A. I. Figueroa, F. Bartolomé, J. Bartolomé, L. M. García, F. Petroff, C. Deranlot, F. Wilhelm, and A. Rogalev, Phys. Rev. B **86**, 064428 (2012).

[9] M. Mogi, T. Nakajima, V. Ukleev, A. Tsukazaki, R. Yoshimi, M. Kawamura, K. S. Takahashi, T. Hanashima, K. Kakurai, T. Arima, M. Kawasaki, and Y. Tokura, Phys. Rev. Lett. **123**, 016804 (2019).

[10] F. Wilhelm, M. Angelakeris, N. Jaouen, P. Poulopoulos, E. T. Papaioannou, C. Mueller, P. Fumagalli, A. Rogalev, and N. K. Flevaris, Phys. Rev. B **69**, 220404(R) (2004).

[11] S. Ruegg, G. Schutz, P. Fischer, R. Wienke, W. B. Zeper, and H. Ebert, J. Appl. Phys. **69**, 5655 (1991).

[12] M. Li, W. Cui, J. Yu, Z. Dai, Z. Wang, F. Katmis, W. Guo, and J. Moodera, Phys. Rev. B **91**, 014427 (2015).

[13] F. Katmis, V. Lauter, F. S. Nogueira, B. A. Assaf, M. E. Jamer, P. Wei, B. Satpati, J. W. Freeland, I. Eremin, D. Heiman, P. Jarillo-Herrero, and J. S. Moodera, Nature (London) **533**, 513 (2016).

[14] C. Swindells, B. Nicholson, O. Inyang, Y. Choi, T. Hase, and D. Atkinson, Phys. Rev. Research **2**, 033280 (2020).

[15] M. Collet, R. Mattana, J. B. Moussy, K. Ollefs, S. Collin, C. Deranlot, A. Anane, V. Cros, F. Petroff, F. Wilhelm, and A. Rogalev, Appl. Phys. Lett. **111**, 202401 (2017).

[16] T. Kikkawa, M. Suzuki, R. Ramos, M. H. Aguirre, J. Okabayashi, K. Uchida, I. Lucas, A. Anadón, D. Kikuchi, P. A. Algarabel, L. Morellón, M. R. Ibarra, and E. Saitoh, J. Appl. Phys. **126**, 143903 (2019).

[17] S. Y. Huang, X. Fan, D. Qu, Y. P. Chen, W. G. Wang, J. Wu, T. Y. Chen, J. Q. Xiao, and C. L. Chien, Phys. Rev. Lett. **109**, 107204 (2012).

[18] S. Geprägs, S. Meyer, S. Altmannshofer, M. Opel, F. Wilhelm, A. Rogalev, R. Gross, and S. T. B. Goennenwein, Appl. Phys. Lett. **101**, 262407 (2012).

[19] Y. M. Lu, Y. Choi, C. M. Ortega, X. M. Cheng, J. W. Cai, S. Y. Huang, L. Sun, and C. L. Chien, Phys. Rev. Lett. **110**, 147207 (2013).

[20] C. Tang, P. Sellappan, Y. Liu, Y. Xu, J. E. Garay, and J. Shi, Phys. Rev. B **94**, 140403(R) (2016).

[21] S. Singh, J. Katoch, T. Zhu, K. Y. Meng, T. Liu, J. T. Brangham, F. Yang, M. E. Flatté, and R. K. Kawakami, Phys. Rev. Lett. **118**, 187201 (2017).

[22] J. C. Leutenantsmeyer, A. A. Kaverzin, M. Wojtaszek, and B. J. Van Wees, 2D Mater. **4**, 014001 (2017).

[23] Z. Wang, C. Tang, R. Sachs, Y. Barlas, and J. Shi, Phys. Rev. Lett. **114**, 016603 (2015).

[24] I. M. Miron, K. Garello, G. Gaudin, P. J. Zermatten, M. V. Costache, S. Auffret, S. Bandiera, B. Rodmacq, A. Schuhl, and P. Gambardella, Nature (London) **476**, 189 (2011).

[25] C. O. Avci, K. Garello, J. Mendil, A. Ghosh, N. Blasakis, M. Gabureac, M. Trassin, M. Fiebig, and P. Gambardella, Appl. Phys. Lett. **107**, 192405 (2015).

[26] F. Büttner, I. Lemesh, M. Schneider, B. Pfau, C. M. Günther, P. Hessing, J. Geilhufe, L. Caretta, D. Engel, B. Krüger, J. Viefhaus, S. Eisebitt, and G. S. D. Beach, Nat. Nanotechnol. **12**, 1040 (2017).

[27] L. Caretta, S.-H. Oh, T. Fakhrul, D.-K. Lee, S. K. Kim, C. A. Ross, K.-J. Lee, and G. S. D. Beach, Science **370**, 1438 (2020).

[28] M. G. Samant, J. Stohr, S. S. P. Parkin, G. A. Held, B. D. Hermsmeier, F. Herman, M. van Schilfgaarde, L.-C. Duda, D. C. Mancini, N. Wassdahl, and R. Nakajima, Phys. Rev. Lett. **72**, 1112 (1994).

[29] A. Hallal, F. Ibrahim, H. Yang, S. Roche, and M. Chshiev, 2D Mater. **4**, 025074 (2017).

[30] W. Amamou, I. V. Pinchuk, A. H. Trout, R. E. A. Williams, N. Antolin, A. Goad, D. J. O'Hara, A. S. Ahmed, W. Windl, D. W. McComb, and R. K. Kawakami, Phys. Rev. Mater. **2**, 011401(R) (2018).

[31] S. Geprägs, C. Klewe, S. Meyer, D. Graulich, F. Schade, M. Schneider, S. Francoual, S. P. Collins, K. Ollefs, F. Wilhelm, A. Rogalev, Y. Joly, S. T. B. Goennenwein, M. Opel, T. Kuschel, and R. Gross, Phys. Rev. B **102**, 214438 (2020).

[32] C. O. Avci, A. Quindeau, M. Mann, C.-F. Pai, C. A. Ross, and G. S. D. Beach, Phys. Rev. B **95**, 115428 (2017).

[33] X. Liang, Y. Zhu, B. Peng, L. Deng, J. Xie, H. Lu, M. Wu, and L. Bi, ACS Appl. Mater. Interfaces **8**, 8175 (2016).

[34] M. B. Jungfleisch, V. Lauer, R. Neb, A. V. Chumak, and B. Hillebrands, Appl. Phys. Lett. **103**, 022411(2013).

[35] Q. Hao, W. Chen, S. Wang, and G. Xiao, J. Appl. Phys. **122**, 033901 (2017).

[36] T. Bublat, and D. Goll, J. Appl. Phys. **108**, 113910 (2010).

[37] R. Pauthenet, J. Appl. Phys. **30**, S290 (1959).

[38] S. Geller, J. P. Remeika, R. C. Sherwood, H. J. Williams, and G. P. Espinosa, Phys. Rev. **137**, A1034 (1965).

[39] H. Tanaka, S. Takayama, and T. Fujiwara, Phys. Rev. B **46**, 7390 (1992).
[40] T. Okuno, D. H. Kim, S. H. Oh, S. K. Kim, Y. Hirata, T. Nishimura, W. S. Ham, Y. Futakawa, H. Yoshikawa, A. Tsukamoto, Y. Tserkovnyak, Y. Shiota, T. Moriyama, K. J. Kim, K. J. Lee, and T. Ono, Nat. Electron. **2**, 389 (2019).
[41] C. O. Avci, E. Rosenberg, J. Mendil, Y. Choi, L. Beran, P. Gambardella, C. A. Ross, and G. S. D. Beach (unpublished).
[42] Y. M. Lu, J. W. Cai, S. Y. Huang, D. Qu, B. F. Miao, and C. L. Chien, Phys. Rev. B **87**, 220409(R) (2013).
[43] E. R. Rosenberg, L. Beran, C. O. Avci, C. Zeledon, B. Song, C. Gonzalez-Fuentes, J. Mendil, P. Gambardella, M. Veis, C. Garcia, G. S. D. Beach, and C. A. Ross, Phys. Rev. Mater. **2**, 094405 (2018).
[44] J. J. Bauer, E. R. Rosenberg, S. Kundu, K. A. Mkhoyan, P. Quarterman, A. J. Grutter, B. J. Kirby, J. A. Borchers, and C. A. Ross, Adv. Electron. Mater. **6**, 1900820 (2020).
[45] A. Quindeau, C. O. Avci, W. Liu, C. Sun, M. Mann, A. S. Tang, M. C. Onbasli, D. Bono, P. M. Voyles, Y. Xu, J. Robinson, G. S. D. Beach, and C. A. Ross, Adv. Electron. Mater. **3**, 1600376 (2017).
[46] M. Althammer, S. Meyer, H. Nakayama, M. Schreier, S. Altmannshofer, M. Weiler, H. Huebl, S. Geprägs, M. Opel, R. Gross, D. Meier, C. Klewe, T. Kuschel, J. M. Schmalhorst, G. Reiss, L. Shen, A. Gupta, Y. T. Chen, G. E. W. Bauer, E. Saitoh, and S. T. B. Goennenwein, Phys. Rev. B **87**, 224401 (2013).
[47] C. F. Majkrzak, K. V. O. Donovan, and N. F. Berk, *Polarized Neutron Reflectometry* (NIST, Gaithersburg, MD, 2004).
[48] H. Zabel, Mater. Today **9**, 42 (2006).
[49] T. Goto, M. C. Onbaşlò, and C. A. Ross, Opt. Express **20**, 28507 (2012).
[50] C. O. Avci, A. Quindeau, C. F. Pai, M. Mann, L. Caretta, A. S. Tang, M. C. Onbasli, C. A. Ross, and G. S. D. Beach, Nat. Mater. **16**, 309 (2017).
[51] B. Maranville, W. Ratcliff II, and P. Kienzle, J. Appl. Cryst. **51**, 1500 (2018).
[52] P. A. Kienzle, B. B. Maranville, K. V. O'Donovan, J. F. Ankner, N. F. Berk, and C. F. Majkrzak, (2017), https://www.nist.gov/ncnr/reflectometry-software.
[53] J. Mendil, M. Trassin, Q. Bu, J. Schaab, M. Baumgartner, C. Murer, P. T. Dao, J. Vijayakumar, D. Bracher, C. Bouillet, C. A. F. Vaz, M. Fiebig, and P. Gambardella, Phys. Rev. Mater. **3**, 034403 (2019).
[54] A. J. Lee, A. S. Ahmed, J. Flores, S. Guo, B. Wang, N. Bagués, D. W. Mccomb, and F. Yang, Phys. Rev. Lett. **124**, 107201 (2020).
[55] L. Caretta, E. Rosenberg, F. Büttner, T. Fakhrul, P. Gargiani, M. Valvidares, Z. Chen, P. Reddy, D. A. Muller, C. A. Ross, and G. S. D. Beach, Nat. Commun. **11**, 1090 (2020).
[56] T. Fakhrul, S. Tazlaru, B. Khurana, L. Beran, J. Bauer, M. Vancik, A. Marchese, E. Tsotsos, M. Kucera, Y. Zhang, M. Veis, and C. A. Ross, Adv. Opt. Mater. **9**, 2100512 (2021).
[57] See Supplemental Material at http://link.aps.org/supplemental/10.1103/PhysRevB.104.094403 for additional structural and magnetic characterization, and additional PNR modeling.
[58] M. Suzuki, H. Muraoka, Y. Inaba, H. Miyagawa, N. Kawamura, T. Shimatsu, H. Maruyama, N. Ishimatsu, Y. Isohama, and Y. Sonobe, Phys. Rev. B **72**, 054430 (2005).
[59] C. J. Kriessman, Rev. Mod. Phys. **25**, 122 (1953).
[60] Q. B. Liu, K. K. Meng, Z. D. Xu, T. Zhu, X. G. Xu, J. Miao, and Y. Jiang, Phys. Rev. B **101**, 174431 (2020).
[61] S. M. Suturin, A. M. Korovin, V. E. Bursian, L. V. Lutsev, V. Bourobina, N. L. Yakovlev, M. Montecchi, L. Pasquali, V. Ukleev, A. Vorobiev, A. Devishvili, and N. S. Sokolov, Phys. Rev. Mater. **2**, 104404 (2018).
[62] J. F. K. Cooper, C. J. Kinane, S. Langridge, M. Ali, B. J. Hickey, T. Niizeki, K. Uchida, E. Saitoh, H. Ambaye, and A. Glavic, Phys. Rev. B **96**, 104404 (2017).
[63] C. Klewe, T. Kuschel, J. M. Schmalhorst, F. Bertram, O. Kuschel, J. Wollschläger, J. Strempfer, M. Meinert, and G. Reiss, Phys. Rev. B **93**, 214440 (2016).
[64] O. Inyang, L. Bouchenoire, B. Nicholson, M. Tokaç, R. M. Rowan-Robinson, C. J. Kinane, and A. T. Hindmarch, Phys. Rev. B **100**, 174418 (2019).
[65] C. Strohm, P. van der Linden, O. Mathon, and S. Pascarelli, Phys. Rev. Lett. **122**, 127204 (2019).
[66] M. Lahoubi, W. Younsi, M. L. Soltani, J. Voiron, and D. Schmitt, J. Phys. Conf. Ser. **150**, 042108 (2009).
[67] M. Lahoubi, W. Younsi, M. L. Soltani, and B. Ouladdiaf, J. Phys. Conf. Ser. **200**, 082018 (2010).
[68] M. Lahoubi and A. Boutaba, in *Proceedings of the 4th International Symposium on Materials and Sustainable Development (ISMSD 2019)*, edited by A. Benmounah, M. T. Abadlia, M. Saidi, and A. Zerizer (Springer, Cham, 2020).